Pulsated Herschel-Bulkley flows in two-dimensional channels: A model for mucus clearance devices

Antoine Galko,[1] Simon Gsell,[2] Umberto D'Ortona,[1] Laurent Morin,[3] and Julien Favier[1,*]
[1]*Aix-Marseille Univ, CNRS, Centrale Marseille, M2P2, Marseille, France*
[2]*Aix Marseille Univ, Université de Toulon, CNRS, CPT (UMR 7332), Turing Centre for Living Systems, Marseille, France*
[3]*Physio-Assist, Montpellier 34090, France*

(Received 18 October 2021; accepted 15 April 2022; published 23 May 2022)

Pressure oscillations applied to human airways can help patients to evacuate bronchial mucus, a highly non-Newtonian gel. To explore the fluid mechanics aspects of these therapies, we perform numerical simulations of pulsated non-Newtonian fluids in two-dimensional channels. The fluid rheology is modeled with the Herschel-Bulkley law, reproducing two essential nonlinear mechanical properties of the mucus, namely, the yield-stress and shear-thinning/thickening properties. The flow dynamics is simulated using the lattice-Boltzmann method over large ranges of the three main nondimensional parameters, i.e., the pulsation rate or Womersley number α, the flow index n quantifying the shear-thinning/thickening effect, and the Bingham number controlling the yield stress. The ratio between the fluctuating and average parts of the oscillatory forcing is examined through three typical cases: a purely oscillating flow, a weakly oscillating flow, and a strongly oscillating flow. For each configuration, specific sets of parameters are found to have a drastic effect on the dynamics of mucus plugs, which suggests new therapeutic strategies for patients suffering from bronchial obstructions.

DOI: 10.1103/PhysRevFluids.7.053301

I. INTRODUCTION

Mucus is a complex biological fluid covering the human respiratory tract and protecting the bronchial epithelium from fine particles and pathogens [1–3]. It is evacuated towards the trachea through the active beating of bronchial epithelial cilia, a process called mucociliary clearance [4,5]. The impairment of this self-defense mechanism is related to a number of respiratory pathologies, such as severe asthma, chronic obstructive pulmonary disease (COPD), and cystic fibrosis. In cystic fibrosis, the bronchial mucus typically tends to dehydrate, becoming viscous, sticky, and difficult to evacuate by natural mechanisms [6,7]. To assist patients in evacuating bronchial mucus, a number of medical devices have been developed [8–10], e.g., vibrating vests or mouth pressure generators [11,12]. All these devices rely on mechanical stresses applied on the bronchi and on the mucus, eventually promoting its expectoration. In particular, mouth pressure generators create internal pressure oscillations propagating along the bronchial tree and presumably altering the mechanical properties of the mucus. Yet the mechanisms involved in the interactions between this complex fluid and such oscillatory perturbations remain unclear.

Performing experiments on real mucus is challenging, because mucus is difficult to collect and it may exhibit variable mechanical properties from one patient to the other. Alternatively, measurements can be done on synthetic fluid models, as in our previous works [13,14] and commonly seen

*julien.favier@univ-amu.fr

in other physical contexts [15]. However, the rheological properties of synthetic fluid models are not always straightforward to characterize and/or to control, and their similarities with real mucus properties are difficult to establish. In this context, numerical simulation is a powerful tool as it allows one to freely investigate the effect of selected and well-controlled rheological properties, which are described through generic mathematical models.

Even though mucus properties generally vary from patient to patient and from one health condition to another [7], it has often been described as a yield-stress shear-thinning fluid[16–18]. Shear-thinning fluids have an effective shear viscosity that tends to decrease as a function of the shear-stress magnitude. In some conditions, mucus can also be a shear-thickening material [19]; in this case, its effective viscosity increases as a function of the shear-stress magnitude. These non-Newtonian fluids can thus be described as Newtonian fluids with nonuniform viscosity, often called generalized Newtonian fluids. As a yield-stress fluid, mucus flows only if the applied shear-stress magnitude is larger than a critical stress; otherwise, it exhibits a solid-like behavior. This property can also be modeled in a generalized Newtonian framework by considering a viscosity that goes to infinity for stresses smaller than the yield stress. Although the mucus typically exhibits additional complex properties as elasticity [20] and thixotropy [18], the present work aims at focusing first on these generalized-Newtonian properties to further understand their role in the mucus dynamics.

In a modeling perspective, pressure waves generated by mucus clearance devices can be thought of as harmonic pressure fluctuations driving non-Newtonian mucus flows in pipe or channel configurations. These oscillatory flows are known as Womersley flows in the Newtonian case. Park and Liu [21] studied the flow of a viscoelastic yield-stress fluid driven by an oscillating pressure gradient, based on experimental and analytical approaches. They emphasized the significant importance of yield-stress and elastic effects in such flows, but their study addressed only limited ranges of physical parameters and did not address the shear-thinning or thickening properties that characterize mucus flows. Womersley flows and non-Newtonian fluids have been widely studied in the context of blood flow modeling. These studies, even though dedicated to systems similar to the one addressed in the present work, cannot be directly used to understand mucus flows since they were performed on ranges of physical parameters (oscillation frequency, flow properties) that were designed to match typical blood flow configurations. We nevertheless cite the works that inspired this work. Sankar and Hemalatha [22] studied numerically the flow of a non-Newtonian fluid in an artery with a catheter, modeled by different generalized-Newtonian models. They used a perturbation method to calculate the flow velocity and the plug size (size of the central solid part), for different oscillation frequencies, controlled through the nondimensional Womersley number α and various fluid properties. They showed that the plug size increases as the yield-stress value increases. Furthermore, Sankar and Lee [23] studied similar flows in a reduced cross section (stenosed) artery and found that the plug core radius, the pressure drop, and the wall shear stress increase with the increase of stenosis heights.

In order to further understand non-Newtonian oscillatory flows relevant in the context of mucus clearance, we explore through two-dimensional numerical simulations the dynamics of a generalized Newtonian fluid driven by an oscillatory body force in a channel. The fluid is modeled by a Herschel-Bulkley law, and the simulations are based on a lattice-Boltzmann method. Simulations are performed over wide ranges of nondimensional frequency (or Womersley number), Bingham number (quantifying the yield-stress effect), and flow index (quantifying the shear-thinning/thickening effect). A focus is placed on three typical configurations, depending on the composition of the oscillatory force signal: (1) a purely oscillating signal (zero-mean body force), (2) a weakly oscillating signal, and (3) a strongly oscillating signal. The system dynamics is systematically explored through the analysis of time-space velocity/viscosity patterns and the study of the instantaneous and time-averaged flow rates.

This paper is organized as follows. The mathematical formulation of the present system is first introduced in Sec. II, and the lattice-Boltzmann method employed to performed the numerical

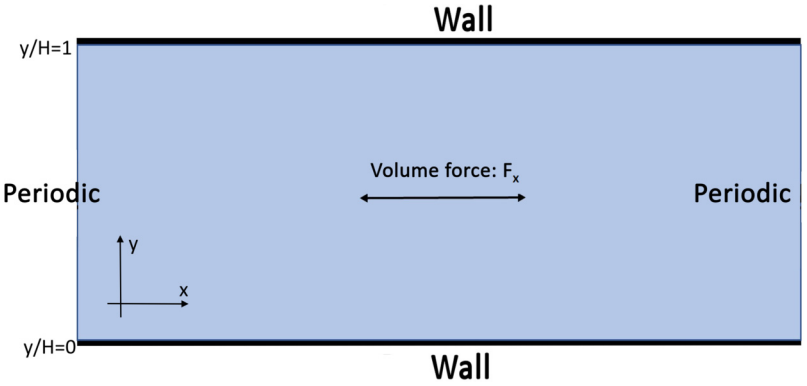

FIG. 1. Scheme of the computational domain.

simulations is detailed in Sec. III. The results are then presented and analyzed in Sec. IV. Finally, the main aspects of this work are summarized in Sec. VI.

II. MATHEMATICAL FORMULATION

A. Governing equations

Let us consider the oscillatory flow of a Herschel-Bulkley fluid in a two-dimensional channel, as schematized in Fig. 1. In the following, the oscillating pressure gradient is replaced by an oscillating body force. Assuming that the flow velocity remains parallel to the x axis and that horizontal gradients $\partial/\partial x$ vanish, the flow dynamics is governed by the one-dimensional momentum equation

$$\rho \frac{\partial u_x}{\partial t} = \frac{\partial \tau}{\partial y} + F_x, \tag{1}$$

where u_x is the velocity along the x axis, F_x is the body force, τ is the viscous shear stress, and ρ is the density. The constitutive equation of a Herschel-Bulkley fluid is given by

$$\begin{cases} \tau = \tau_0 + K\dot{\gamma}(|\dot{\gamma}|)^{n-1} & \text{for} \quad |\tau| > \tau_0 \\ \dot{\gamma} = 0 & \text{for} \quad |\tau| < \tau_0 \end{cases}, \tag{2}$$

where $\dot{\gamma}$ is the shear rate $\partial u_x/\partial y$, τ_0 is the yield stress, K is the consistency parameter (units Pa s^n), and n is the flow index. This equation can model two types of behavior depending on the value of n. If $n < 1$, the fluid exhibits a shear-thinning behavior (i.e., the viscosity decreases when the shear stress increases), and if $n > 1$ the fluid is shear-thickening (i.e., the viscosity increases when the shear stress increases). When $\tau < \tau_0$, the shear vanishes and the "fluid" medium behaves like a "solid." Following a generalized-Newtonian approach, the shear stress is modeled as

$$\tau = \mu(|\dot{\gamma}|)\dot{\gamma}, \tag{3}$$

where μ is the apparent fluid viscosity, which takes a limit but large value in solid-like regions [Eq. (4)]. In the following, the Herschel-Bulkley model is adapted to our numerical framework by introducing a very high viscosity associated with the solid-like regions of the flow:

$$\begin{cases} \mu_{\text{eff}}^{\text{liq}} = \frac{\tau_0}{\dot{\gamma}} + K(|\dot{\gamma}|)^{n-1} & \text{for} \quad |\dot{\gamma}| > \dot{\gamma}_0 \\ \mu_{\text{eff}}^{\text{sol}} = \mu_{\text{sol}} & \text{for} \quad |\dot{\gamma}| < \dot{\gamma}_0 \end{cases}, \tag{4}$$

where $\mu_{\text{eff}}^{\text{liq}} \ll \mu_{\text{eff}}^{\text{sol}}$ and $\dot{\gamma}_0$ is the characteristic shear rate related to the yield stress τ_0. In many numerical studies, infinite viscosities are avoided by using a regularized Herschel-Bulkley law [24].

In the present work, a simple truncation is employed, and no significant alteration of the results has been observed.

The oscillatory force driving the flow is expressed as

$$F_x = g_x[\xi_1 + \xi_2 \cos(\omega t)], \tag{5}$$

where g_x is the characteristic magnitude of the force, ξ_1 and ξ_2 are two nondimensional parameters controlling the form of F_x, and ω is the pulsation. Based on this definition, three typical cases are considered: the purely oscillating force ($\xi_1 = 0$), the weakly oscillating force ($\xi_1 \gg \xi_2$), and the strongly oscillating force ($\xi_1 \ll \xi_2$).

Equation (1) can be made dimensionless by defining the following nondimensional quantities:

$$u_x^* = \frac{u_x}{U_0}, y^* = \frac{y}{H}, t^* = \omega t, \tau^* = \frac{\tau}{\tau_{\text{ref}}}, \tag{6}$$

where U_0 is defined by $U_0 = \sqrt{g_x H/\rho}$ and $\tau_{\text{ref}} = \mu_{\text{ref}}\dot{\gamma}_0$ is the reference shear stress with μ_{ref} a reference viscosity. Using Eq. (5) and dropping the stars, Eq. (1) becomes

$$\alpha^2 \frac{\partial u_x}{\partial t} = \text{Re}[\xi_1 + \xi_2 \cos(t)] + \frac{\partial \tau}{\partial y}, \tag{7}$$

where α is the Womersley number defined by $\alpha = H\sqrt{\frac{\rho\omega}{\mu_{\text{ref}}}}$, and the Reynolds number is defined by $\text{Re} = \frac{\rho U_0 H}{\mu_{\text{ref}}}$ [21].

Analytical solutions of equation (7) exist for particular cases. As an illustration, solutions for the steady Poiseuille non-Newtonian flow and the Womersley Newtonian flow will be examined in the next section.

B. Analytical solutions

1. Poiseuille non-Newtonian flow

If the flow is driven by a constant body forcing ($\xi_1 = 1, \xi_2 = 0$), the steady flow solution satisfies

$$0 = \text{Re} + \frac{\partial \tau}{\partial y}. \tag{8}$$

Using the truncated Herschel-Bulkley law described by Eq. (4), the analytical solution reads [25]

$$\begin{cases} u_x = \frac{-n}{n+1}\text{Re}^{\frac{1}{n}}\left(-y + 0.5 - \frac{\text{Bn}}{\text{Re}}\right)^{\frac{n+1}{n}} + \frac{n}{n+1}\text{Re}^{\frac{1}{n}}\left(0.5 - \frac{\text{Bn}}{\text{Re}}\right)^{\frac{n+1}{n}} & \text{for} \quad y \leqslant y_0 \\ u_x = \frac{\text{Re}^\star}{2}(y - y^2) + u_x(y_0) & \text{for} \quad y_0 \leqslant y \leqslant 1 - y_0 \end{cases}, \tag{9}$$

where y_0 is the position of the interface between fluid-like and solid-like regions, $\text{Re}^\star = \frac{\rho U_0 H}{\mu_{\text{sol}}}$ is the Reynolds number associated with the "solid" part, and $\text{Bn} = \frac{\sigma_0}{K}(\frac{H}{U_0})^n$ is the Bingham number where σ_0 is the yield stress, quantifying the ratio between the yield stress and the viscous strain. The solution in the range $y \geqslant 1 - y_0$ can be obtained by replacing $-y + 0.5 - \text{Bn/Re}$ by $y - 0.5 - \text{Bn/Re}$ in the upper line of Eq. (9). The analytic solution consists of two parts, the liquid part and the plug part. In the case of a solid with infinite viscosity, the position of the interface reads $y_0 = 0.5 - \text{Bn/Re}$. It is recalled that the plug part is not exactly solid, as is described using a highly viscous fluid [see (4)]. As a consequence, a correction appears in y_0 that is usually very small. The analytical flow described by Eq. (9) is depicted in Fig. 2 for $\mu_r = 2500$, $\text{Re} = 10$, $\text{Bn/Re} = 3/10$, and $n = 1$. We define here $\mu_r = \mu_{\text{sol}}/\mu_{\text{liq}}$, the ratio between the reference viscosities of the solid-like and fluid-like regions. Details of the choice of μ_r are given in Sec. IV A. The two flow regions are clearly identified. In high-shear regions, close to the channel walls, the flow exhibits a fluid behavior. In the low-shear region, a plug develops and the flow exhibits a solid-like behavior. Note that the plug size increases as a function of Bn. Due to the fluid modeling of the solid region, the

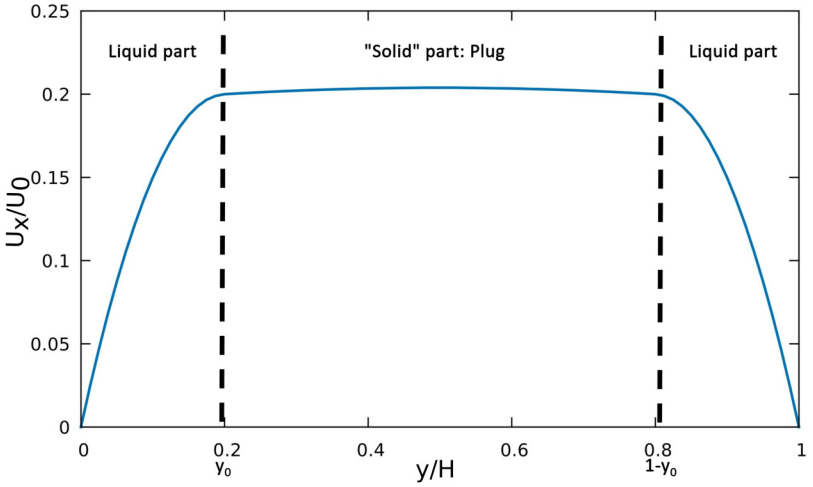

FIG. 2. Analytical solution for the Herchel-Bulkley flow driven by a constant body force, Bn/Re = 3/10, $n = 1$, and $\mu_r = 2500$; see Eq. (9).

flow profile is not exactly flat across the central plug. However, when the viscosity ratio μ_r is large enough, the plug behavior is well reproduced, as shown in Fig. 2.

2. *Womersley Newtonian flow*

When the flow is Newtonian, Eq. (7) becomes

$$\alpha^2 \frac{\partial u_x}{\partial t} = \mathrm{Re}[\xi_1 + \xi_2 \cos(t)] + \frac{\partial^2 u_x}{\partial y^2}, \tag{10}$$

and the analytical solution derived by Womersley [26] is

$$U(y,t) = \frac{\mathrm{Re}\xi_1}{2}(y - y^2) + \mathrm{Real}\left\{\frac{\mathrm{Re}\xi_2}{i\omega}\left[1 - \frac{\cosh\left(t\,(y-0.5)\frac{\alpha}{\sqrt{2}}\right)}{\cosh\left(\frac{t}{2\sqrt{2}}\right)}\right]\right\}.$$

Figure 3 shows an example of the velocity profile for $\mathrm{Re} = 0.1$ and $\alpha = 5$ for a series of time steps $t = n\pi/8$, with $n = \{0, \ldots, 15\}$, i.e., encompassing one oscillating period. In this example, $\xi_1 = 0$ and the flow profile is thus symmetrically reversed at each half period. When α is high, a phase shift develops between the velocities at the center of the channel and those close to the walls.

Even though the above analytical solutions are well known, there is no analytical solution for non-Newtonian fluids in Womersley flow, and therefore, a numerical strategy is proposed in the following.

III. NUMERICAL METHOD

In the following, the unsteady flow dynamics (1) is predicted on the basis of lattice-Boltzmann (LB) simulations. As the flow is expected to remain one-dimensional, simulations are performed in a two-dimensional periodic channel with only three nodes along the flow direction. In the LB method, the flow dynamics is described through the particle distribution function $f(\boldsymbol{x}, \boldsymbol{\xi}, t)$, which represents the density of fluid particles moving with velocity ξ at location $\boldsymbol{x}$ and time t. The dynamics of the distribution function is governed by the Boltzmann equation,

$$\frac{\partial f}{\partial t} + \boldsymbol{\xi} \cdot \nabla f = \Omega(f), \tag{11}$$

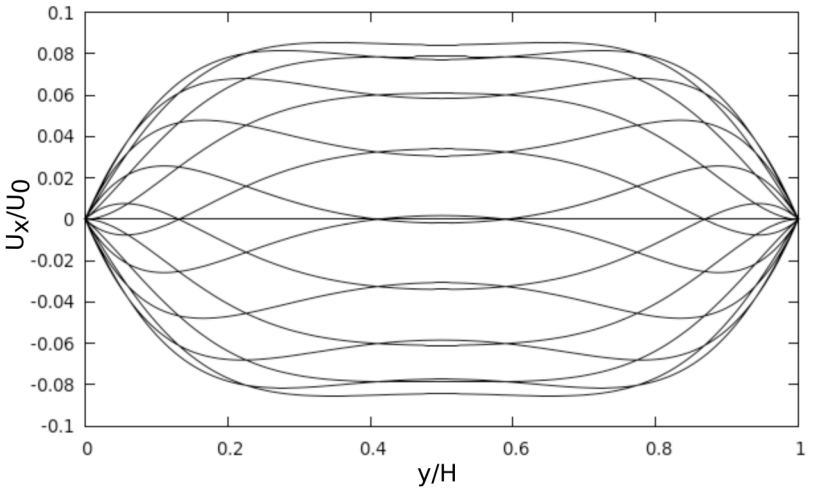

FIG. 3. Analytical solution of the Newtonian oscillatory flow (Womersley flow) in a channel, for $\xi_1 = 0$, $\xi_2 = 1$, $\alpha = 5$, Re $= 0.1$ at $t = n\pi/8$ for $n = [0 : 15]$; see Eq. (11).

where Ω is the collision operator. The discretization of Eq. (11) in velocity space, physical space, and time leads to the LB equation. The velocity space is discretized on a set of velocity vectors $\{\mathbf{e}_i, i = 0,...,Q-1\}$ where Q is the number of discrete velocities. The discretization model used in the present work is the D_2Q_9 scheme, in which the velocity space is discretized by nine velocities,

$$\mathbf{e}_i = \begin{cases} (0,0), & i = 0, \\ c\left(\cos\left[\frac{\pi(i-1)}{2}\right],\ \sin\left[\frac{\pi(i-1)}{2}\right]\right), & i \in [1,4], \\ \sqrt{2}c\left(\cos\left[\frac{\pi(2i-9)}{4}\right],\ \sin\left[\frac{\pi(2i-9)}{4}\right]\right), & i \in [5,8], \end{cases} \tag{12}$$

where c is the lattice velocity. The particle densities at velocities $\mathbf{e}_i$ are represented by the particle populations $f_i(\mathbf{x}, t)$. Time and space are discretized so that particle populations are transported from one node to the neighboring one during one time step, namely, $\Delta x/\Delta t = \Delta y/\Delta t = c$. The spatial grid is Cartesian and uniform, namely, $\Delta x = \Delta y$ are constant. In the following all the quantities are normalized by c and Δt, namely, $\Delta x = \Delta y = \Delta t = 1$. Using this normalization, the LB equation reads

$$f_i(\mathbf{x} + \mathbf{e}_i, t+1) - f_i(\mathbf{x}, t) = \Omega_i(\mathbf{x}, t) + S_i(\mathbf{x}, t), \tag{13}$$

where S_i is the contribution of an external body force term. The left-hand side of Eq. (13) is called the streaming step and the right-hand side is the collision. Equation (13) is explicit, and the streaming and collision steps can thus be treated separately.

The macroscopic quantities, ρ the density and $\mathbf{u}$ the velocity, are computed as moments of the particle functions in the velocity space [27]

$$\rho\mathbf{u} = \textstyle\sum_{i=0}^{8} f_i\mathbf{e}_i + \frac{1}{2}S_i \tag{14}$$

with S_i expressed as

$$S_i = \left(1 - \frac{1}{2\tau}\right) w_i \left[\frac{\mathbf{e}_i - \mathbf{u}}{c_s^2} + \frac{(\mathbf{e}_i \cdot \mathbf{u})\mathbf{e}_i}{c_s^4}\right] \cdot \mathbf{F}, \tag{15}$$

where $\boldsymbol{F} = (F_x, 0)$ is the macroscopic body force, c_s is the lattice sound speed equal to $1/\sqrt{3}$ using the present normalization, and w_i are the weights specific to the velocity set. In the present case (D_2Q_9), $w_0 = 4/9$, $w_i = 1/9$ for $i = 1, 2, 3, 4$, and $w_i = 1/36$ for $i = 5, 6, 7, 8$.

The collision operator relaxes the distributions $\{f_i\}$ towards the equilibrium distributions $f_i^{\mathrm{eq}}(\rho, \boldsymbol{u})$ defined as

$$f_i^{\mathrm{eq}}(\mathbf{x}, t) = w_i \rho \left[1 + \frac{\mathbf{e}_i \cdot \mathbf{u}}{c_s^2} + \frac{(\mathbf{e}_i \cdot \mathbf{u})^2}{2c_s^4} - \frac{\mathbf{u}^2}{2c_s^2} \right]. \tag{16}$$

In this work, a two-relaxation-time collision operator is employed,

$$\Omega_i = -\frac{1}{\tau^+}\left(f_i^+ - f_i^{\mathrm{eq}+}\right) - \frac{1}{\tau^-}\left(f_i^- - f_i^{\mathrm{eq}-}\right), \tag{17}$$

where τ^+ and τ^- are two relaxation times associated with the relaxation of symmetric and antisymmetric populations, defined as

$$\begin{cases} f_i^+ = \frac{f_i + f_{\bar{i}}}{2}, & f_i^- = \frac{f_i - f_{\bar{i}}}{2}, \\ f_i^{\mathrm{eq}+} = \frac{f_i^{\mathrm{eq}} + f_{\bar{i}}^{\mathrm{eq}}}{2}, & f_i^{\mathrm{eq}-} = \frac{f_i^{\mathrm{eq}} - f_{\bar{i}}^{\mathrm{eq}}}{2}. \end{cases} \tag{18}$$

The symmetric relaxation time τ^+ determines the macroscopic kinetic fluid viscosity $\nu = c_s^2(\tau^+ - \frac{1}{2})$. The antisymmetric relaxation time τ^- is a free numerical parameter. The latter is controlled through the parameter $\Lambda = (\tau^+ - 0.5)(\tau^- - 0.5)$, which should be kept constant locally in order to ensure the viscosity independence of the bulk flow dynamics [28,29]. In the following, Λ is set to $1/4$ [30].

The non-Newtonian behavior of the fluid is modeled through local variations of the shear-dependent fluid viscosity. In LB simulations, the shear rate can be computed locally through [31]

$$\mathcal{S}_{\alpha\beta} = -\frac{3}{2\rho\tau^+} \sum_{i=0}^{8} f_i^{\mathrm{neq}} e_{i\alpha} e_{i\beta}, \tag{19}$$

where f_i^{neq} is the nonequilibrium part of the particle functions defined as $f_i^{\mathrm{neq}} = f_i - f_i^{\mathrm{eq}}$.

In non-Newtonian simulations, τ^+ may be time-dependent; in this case the value of τ^+ issued from the previous time step is used in Eq. (19). Based on the generalized-Newtonian constitutive Eq. (4), the local relaxation time is

$$\tau^+(\mathbf{x}, t) = \frac{\tau_0 \dot{\gamma}^{-1} + K \dot{\gamma}^{n-1}}{\rho c_s^2} + \frac{1}{2}, \tag{20}$$

where $\dot{\gamma} = \sqrt{2(\mathcal{S}_{11}^2 + 2\mathcal{S}_{12}^2 + \mathcal{S}_{22}^2)}$. At each time step, the value of τ^+ is determined according to Eq. (20) and τ^- is updated is order to keep Λ constant.

Simulations are performed in a periodical channel, and the no-slip condition at the walls is ensured by a nonequilibrium bounce-back scheme [32]. Among all the performed simulations, the range of the viscosity at the wall is $\mu_{\mathrm{eff}} \in [0.0033, 8.33]$ but the velocity slip remains low $U_{\mathrm{wall}} \leqslant 10^{-5}$.

IV. NUMERICAL RESULTS

The first part of this section focuses on the validation of the numerical solver using the two test cases presented in Sec. II. The second part is dedicated to the study of the oscillatory flow of a Herschel-Bulkley fluid in a two-dimensional channel for three different configurations: a purely oscillatory flow, a weakly oscillating flow, and a strongly oscillating flow.

A. Validation of the solver

We first consider the simulation of a Herschel-Bulkley flow driven by a constant body force. The impact of the viscosity ratio μ_r involved in the generalized-Newtonian rheology (4) is examined in Fig. 4. In these simulations, the value of τ_{min} (minimal relaxation time) is equal to 0.51, and τ_{max}

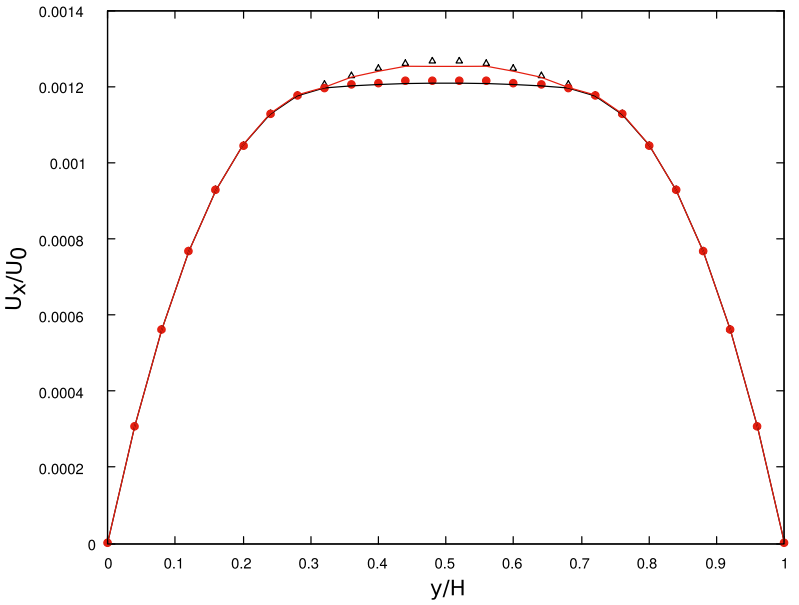

FIG. 4. Impact of the viscosity ratio on the velocity profile for Re = 0.1, Bn/Re = 0.15, $n = 0.7$, △: $\mu_r = 500$, •: $\mu_r = 1500$, black line: $\mu_r = 2500$, and red line: $\mu_r = 3500$.

(maximal relaxation time) is varied through μ_r. The value of μ_r is derived by obtaining μ_{liq} as $\mu_{\text{liq}} = \frac{c_s^2}{\rho}(\tau_{\text{min}} - 0.5)$. The optimal ratio μ_r is defined in the following. As discussed in Fig. 2, the flow exhibits a nearly solid plug at the center of the channel. The numerical accuracy in the plug region is closely related to the value of μ_r. When μ_r is small, a shear clearly appears in the plug region. Even though the present numerical approach is accurate over a large range of viscosities, numerical errors are expected to emerge for very large viscosities [28]. This error is illustrated in Fig. 4; when μ_r is too large ($\mu_r = 3500$), it deteriorates the value of the velocity because the value of the maximal truncation τ_{max} likely becomes too high. For example, in the case of $\mu_r = 3500$ the value of τ_{max} is equal to 35.5. In this case, the value of the relaxation time becomes too high and the accuracy decreases. The optimal value of μ_r is found to be $\mu_r = 2500$, resulting in a nonsheared plug region without discontinuity.

The mesh resolution must be sufficient to capture the sharp viscosity variation between the solid-like and fluid-like regions. In the following, the grid spacing is set to $\Delta x/H = 0.01$ after a convergence study indicating that for lower values of $\Delta x/H$, the velocity profile remains unaltered.

Figures 5(a) and 5(b) show a series of velocity profiles simulated in the case of the steady channel flow for different values of Bn and n. The numerical parameters used are $\tau_{\text{min}} = 0.51$ and $\mu_r = 2500$. The numerical flow profiles are in agreement with the analytical ones for all values of n and Bn.

The reliability of the solver in simulating oscillatory flow in the Newtonian case is illustrated in Figs. 6(a) and 6(b), where numerical simulations are compared to analytical ones for two values of the Womersley number α. An excellent agreement is noted in both cases. The numerical time step is fixed for each simulation to satisfy the stability constraints of the LB method [31]. The number of time iterations of the solver is larger than 200 000 per oscillation period.

We have performed additional simulations to confirm that the flow is not affected by the periodic boundary conditions along the x direction. In particular, simulation performed with a channel length $L = 10H$, $\alpha = 7$, and large Bingham numbers have shown that the flow remains one-dimensional.

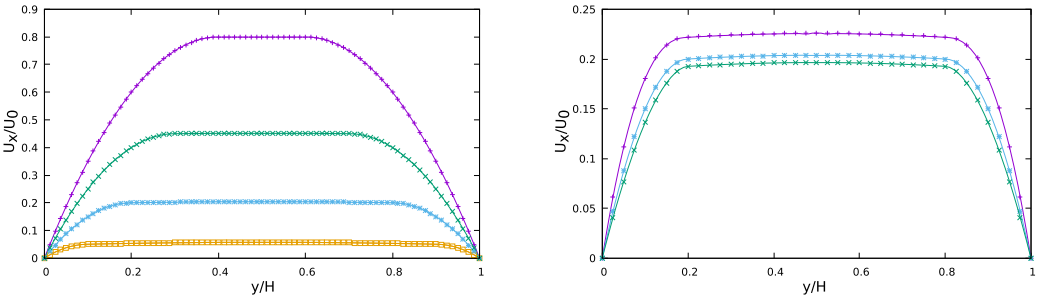

(a) (b)

FIG. 5. Velocity profiles (a) Re = 10, $n = 1$ and different Bn, purple: Bn = 1, green: Bn = 2, blue: Bn = 3, yellow: Bn = 4; (b) Re = 10, Bn = 3, purple: $n = 0.7$, blue: $n = 1$, green: $n = 1.3$. The lines represent the analytical solutions, and the symbols the numerical ones.

In the following simulations, a quasi-one-dimensional channel is thus considered, with L equal to three nodes.

V. RESULTS AND DISCUSSION

In the following, we examine the numerical results for three typical flows corresponding to (1) a purely oscillating flow, (2) a weakly oscillating flow, and (3) a strongly oscillating flow. A focus is placed on the case Re = 0.1 and $n = 1.3$. Results obtained for $n = 0.7$ are presented in the Appendix. In the following, the Reynolds number is fixed to Re = 0.1, and the Bingham number is varied through the ratio Bn/Re. Indeed, Eq. (9) shows that this ratio controls the plug size in the steady flow case. In particular, the flow completely vanishes when Bn/Re $\geqslant 0.5$. This parameter is thus chosen as the relevant one to characterize the competition between the driving force and the yield stress.

A. Purely oscillating flow

We first examine the purely oscillating flow, i.e., the flow driven by a zero-mean oscillatory force. Figures 7(a) and 7(b) show the velocity profiles in the channel at different instants for two pulsation rates $\alpha = 1$ and $\alpha = 7$. The ratio Bn/Re limits the yield stress values for the study between 0 (no yield stress) and 0.5 (the plug cannot be yielded). Compared to the Newtonian case depicted in Figs. 6(a) and 6(b), the yield-stress fluid flows are characterized by the presence of a solid-like

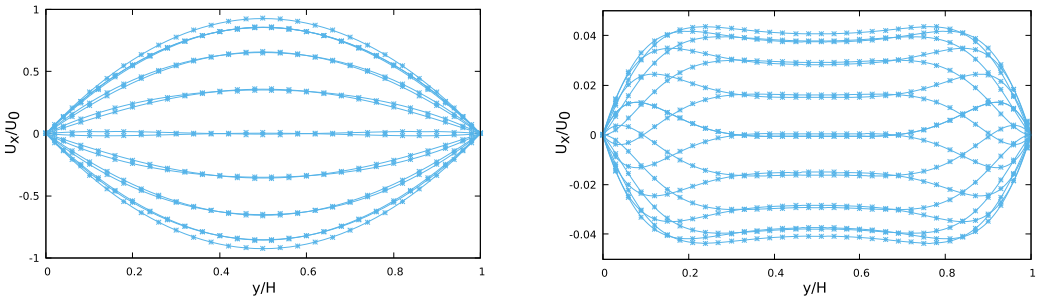

(a) (b)

FIG. 6. Newtonian oscillatory flow for (a) Re = 10, $\alpha = 1$ and (b) Re = 10, $\alpha = 7$: numerical (symbols) and analytical (solid lines) velocity profiles at times $t = n\pi/8$ and $n = \{0, \ldots, 15\}$.

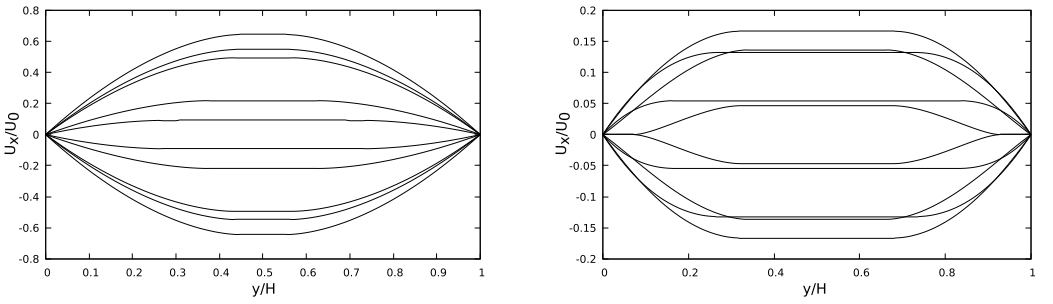

(a) (b)

FIG. 7. Velocity profile for $n\,2\pi/10$, for n being an integer number between 0 and 9 (a) $\mathrm{Re} = 0.1$, $\mathrm{Bn/Re} = 0.05$, $\alpha = 1$, and $n = 1.3$; (b) $\mathrm{Re} = 0.1$, $\mathrm{Bn/Re} = 0.05$, $\alpha = 7$, and $n = 1.3$.

zero-shear region at the center of the channel. In steady flows, the size of the plug is determined by the ratio $\mathrm{Bn/Re} \sim U_0^{-2}$, as shown by the analytical solution (9). Based on a pseudosteady approach, one might thus expect the plug size in unsteady flows to vary as a function of the instantaneous nominal velocity $U_0(t) \sim \sqrt{F(t)}$. This is qualitatively observed in Figs. 7(a) and 7(b), where the plug size tends to be larger during low-velocity periods, i.e., when the instantaneous oscillating force $F(t)$ is small. The peak velocity in the channel also tends to decrease at large pulsation rates; consequently, the plug size tends to be larger in these cases.

A broader visualization of the time evolution of the flow velocity as a function of the Bingham number and pulsation rate is proposed in Fig. 8. For each value of the $[\alpha, \mathrm{Bn/Re}]$ parameter space, the flow is visualized using isocontours of the velocity as a function of time and space, over one oscillating period. Each space-time diagram is obtained by considering one line perpendicular to the flow direction, coloring the value of interest (velocity or viscosity) and assembling horizontally the evolution of the line over time. In this plot and in the following, the time axis is set so that the

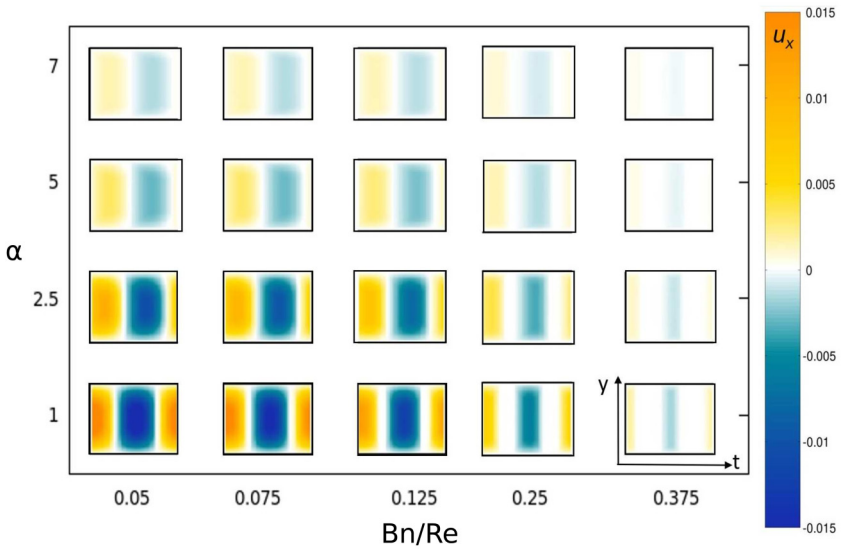

FIG. 8. Space-time diagram of the velocity field during one period for each pair of dimensionless numbers α, Bn/Re and $n = 1.3$. The velocity magnitude is indicated by the color bar. For each subplot, the x axis corresponds to the temporal evolution, and the y axis gives the position inside the channel.

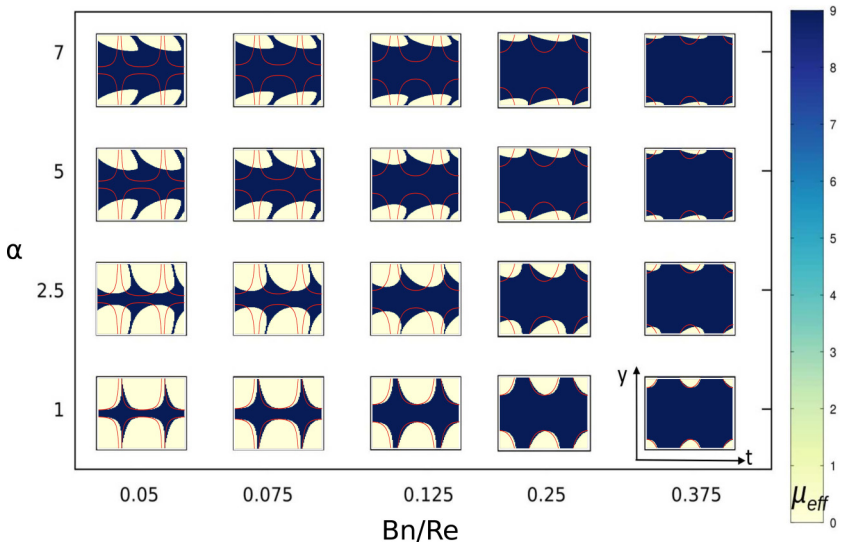

FIG. 9. Space-time diagrams of dynamic viscosity during one period for each pair of dimensionless numbers α, Bn/Re and $n = 1.3$. For each subplot, the x axis corresponds to the temporal evolution, and the y axis gives the position inside the channel. The blue part represents the "solid" behavior of the fluid, while the white part represents the liquid part. The red line corresponds to the position of the interface $y_{i0}(t)$.

driving force is maximal at $t = 0$. As expected from the analytical solution in the steady case (9), the peak velocity in the channel significantly decreases as the yield stress τ_0 increases (i.e., Bn/Re increases). As commented above, the plug size is expected to vary as a function of the instantaneous nominal velocity related to the oscillating force. When the oscillating force is small enough, the plug extends across the whole channel, resulting in temporary quiescent flows emphasized by the white regions in Fig. 8. The typical duration of these quiescent periods increases as a function of Bn/Re; for Bn/Re $\geqslant 1/2$, the flow completely vanishes.

The effect of the physical parameters on the plug dynamics is further examined in Fig. 9, which shows isocontours of the effective viscosity over time and space, for different values of α and Bn/Re. In this figure, blue regions indicate solid-like parts of the flow. The time evolution of the plug size, already commented above, is clearly noted in the figure. All simulations exhibit a transient quiescent state, whose duration increases as a function of Bn/Re. The plug size is also generally larger at high pulsation rates, as previously observed in Figs. 7(a) and 7(b). When the flow is quasisteady, the position of the fluid-solid interface can be predicted based on the analytical solution given by Eq. (9). The quasisteady interface position (red lines in Fig. 9) is $y_{i0}(t) = 1/2 - \mathrm{Bn}_i(t)/\mathrm{Re}_i(t)$, where Bn_i and Re_i are the instantaneous Bingham and Reynolds numbers based on the instantaneous nominal velocity $U_0(t) = \sqrt{F_x(t)H/\rho}$. As shown in Fig. 9, y_{i0} accurately predicts the plug dynamics for small values of α. In contrast, unsteady effects are clearly noted for $\alpha \geqslant 2.5$; these effects are especially characterized by the emergence of a cross-flow phase shift in the viscosity dynamics.

In the present configuration, the time-averaged body force vanishes, and so does the time-averaged flow rate. Yet the instantaneous flow rate can significantly depart from zero, and its maximum value is affected by the physical parameters. This is examined in Figs. 10(a) and 10(b), where the maximum flow rate is plotted as a function of Bn/Re for different values of α and n. It is compared to the corresponding quasisteady flow rate, i.e., the flow rate of a steady Poiseuille flow with the same values of Bn/Re and n. Overall, the maximal flow decreases when the Womersley number increases and when the yield stress increases. When $\alpha = 1$ the max flow rate nearly matches the pseudosteady flow rate. In contrast, an increase of the oscillation frequency leads to substantial

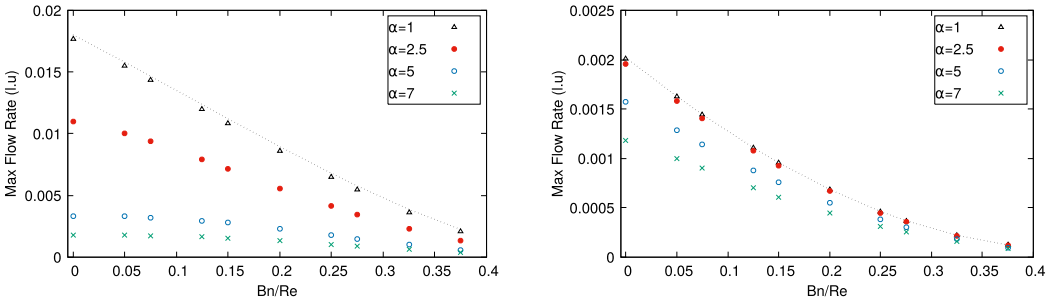

FIG. 10. Maximal flow rate in lattice units (l.u.) for each pair of (α, Bn/Re) and (a) $n = 1.3$ and (b) $n = 0.7$. Dotted line: flow rate for Poiseuille flow.

deviations from the quasistatic case, and the maximal flow rate tends to vanish. This effect can be understood as a result of the short timescale separation between the oscillating force and the fluid inertia. The maximal flow rate also tends to vanish as Bn/Re increases as a result of the plug size growth. It can be noted that the maximal flow rate is 10 times lower for $n = 0.7$ compared to $n = 1.3$. For low Reynolds number, here $\mathrm{Re} = 0.1$, the shear-thickening fluid thus flows faster than the shear-thinning one. Moreover the impact of the oscillation is reduced for $n = 0.7$: the maximal ratio between the pseudosteady and unsteady flow rates is 1.6 against 9 for $n = 1.3$.

As commented in Fig. 3, high-frequency oscillations of the driving force can lead to substantial variations of the velocity phase across the channel. This mechanism is associated with the emergence of a phase difference between the overall flow rate in the channel and the driving force. This is illustrated in Fig. 11, where the phase difference is plotted as a function of α and Bn/Re. Here the phase lag is determined based on the Fourier transform of the flow rate signal, using the force signal as the reference phase. As in the Newtonian case, the phase shift is found to increase with α. Moreover, it is noted that the phase difference significantly decreases as a function of Bn/Re: the yield-stress effect tends to synchronize the flow with the driving force. This can be understood by

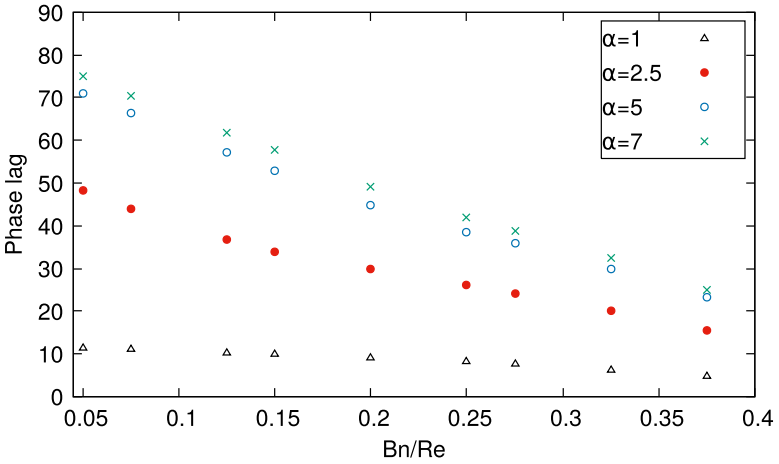

FIG. 11. Phase lag (in degrees) between the driving force and the flow rate for each pair of (α, Bn/Re) and $n = 1.3$.

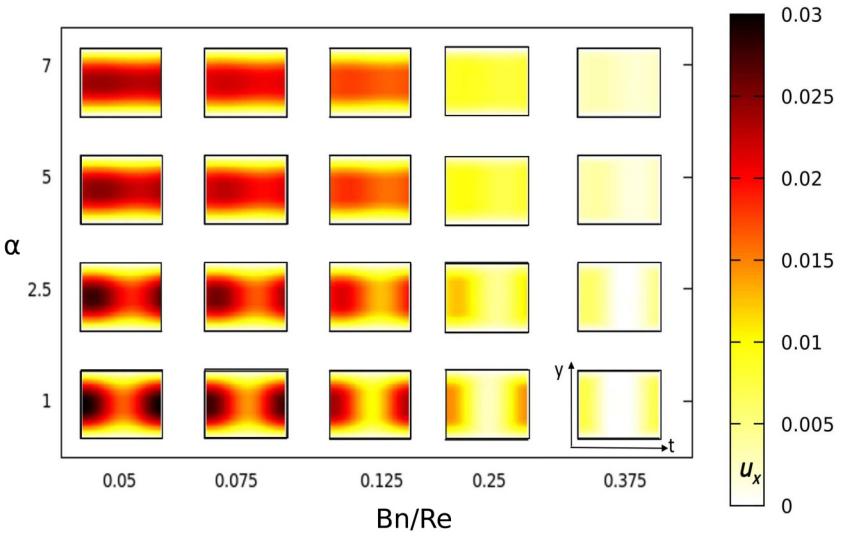

FIG. 12. Space-time diagrams of the velocity during one period of oscillation for each pair of α, Bn/Re and $n = 1.3$.

considering the fact that the yield-stress effect tends to increase to the overall fluid viscosity across the channel, decreasing the effective Womersley number and the associated phase difference.

B. Weakly oscillating flow

In the following, we consider a driving oscillatory force composed of a large time-averaged contribution and a small fluctuating part. This is achieved by setting $\xi_2/\xi_1 = 0.3$, where ξ_1 and ξ_2 are defined in Eq. (5). An overview of the time evolution of the flow velocity as a function of α and Bn/Re is provided in Fig. 12. As a result of the weakly oscillating form of the driving force, the flow velocity remains always positive in the channel (hence velocity contours are plotted using a sequential color scheme in the figure). As already observed in the purely oscillatory case, the amplitude of velocity fluctuations tends to decrease with α. At large pulsation rates, velocity variations become negligible compared to the time-averaged part of the flow, and the flow thus becomes nearly steady. Even though the time-averaged force prevents the emergence of negative velocities, the yield stress effect can be strong enough to develop plugs that periodically stop the flow, as emphasized by the zero-velocity (white) regions in Fig. 12.

This is confirmed in Fig. 13, where a channel-size plug is observed for Bn/Re $= 0.375$ at small pulsation rates. In other cases, the solid-like region is only observed at the center of the channel, with a width that depends on α and Bn/Re and that may vary as a function of time. As observed for the velocity contours in Fig. 12, the flow tends to become steady at large pulsation rates, resulting in a steady central plug.

The evolution of the time-averaged flow rate is plotted in Figs. 14(a) and 14(b). When the flow dynamics is linear, i.e., when Bn $= 0$ and $n = 1$, the superposition principle implies that the average flow rate should be equal to a linear combination of contributions related to the mean and fluctuating parts of the driving force. Since the latter contribution vanishes on average, in linear dynamics the time-averaged flow rate should be equal to the flow rate resulting from the time-averaged force. Here, even though the dynamics of the flow is nonlinear, the oscillating part of the driving force is too small to result in significant nonlinear effect. This is clearly observed in Figs. 14(a) and 14(b), where the flow rate remains close to the steady one, although small deviations are noted for strongly

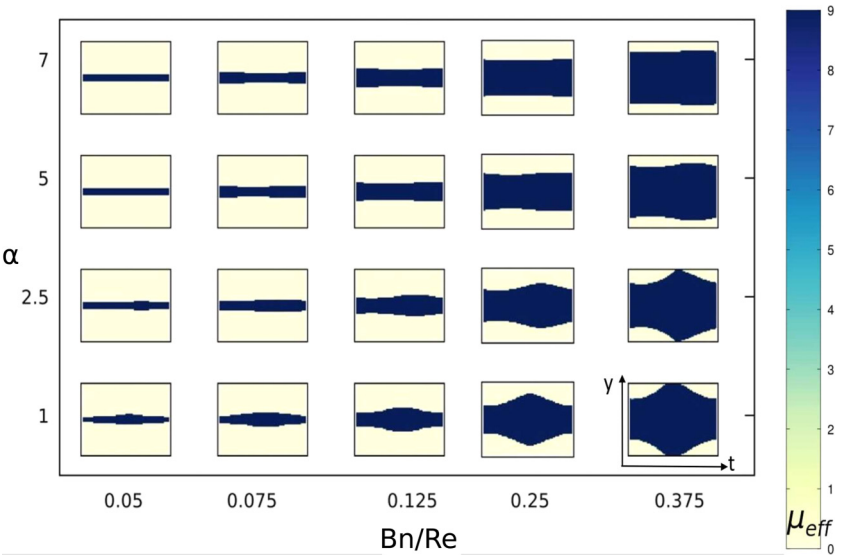

FIG. 13. Space-time diagram of the dynamic viscosity during one period of oscillation for each pair of α, Bn/Re and $n = 1.3$. For each subplot, the x axis corresponds to the temporal evolution, and the y axis is the position inside the channel. The blue part represents the "solid" behavior of the fluid, while the white part represents the liquid part.

nonlinear flows (i.e., large values of Bn/Re). The value of the flow index n has no effect on this behavior; however, the mean flow rate is drastically larger for shear-thickening fluids.

C. Strongly oscillating flow

The last typical case analyzed here is characterized by an oscillatory force composed of a small time-averaged contribution with large-amplitude fluctuations, i.e., $\xi_1/\xi_2 = 0.3$. In this case, the resulting oscillatory flow may be either positive or bidirectional, depending on the oscillation rate. The evolution of the flow velocity is shown in Fig. 15. As observed in the weakly oscillating case, the oscillatory part of the flow tends to vanish for large values of α due to inertial effects. In this case, the flow remains positive over the oscillation period. Figure 16 shows that the plug dynamics strongly depends on α and Bn/Re. For small values of α, the plug size varies as a function of

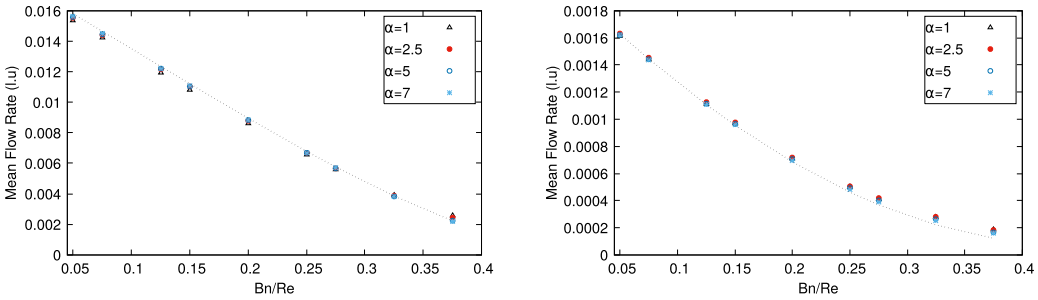

FIG. 14. Mean flow rate for each pair of (α, Bn/Re) and (a) $n = 1.3$ and (b) $n = 0.7$. Dotted line: flow rate for Poiseuille flow

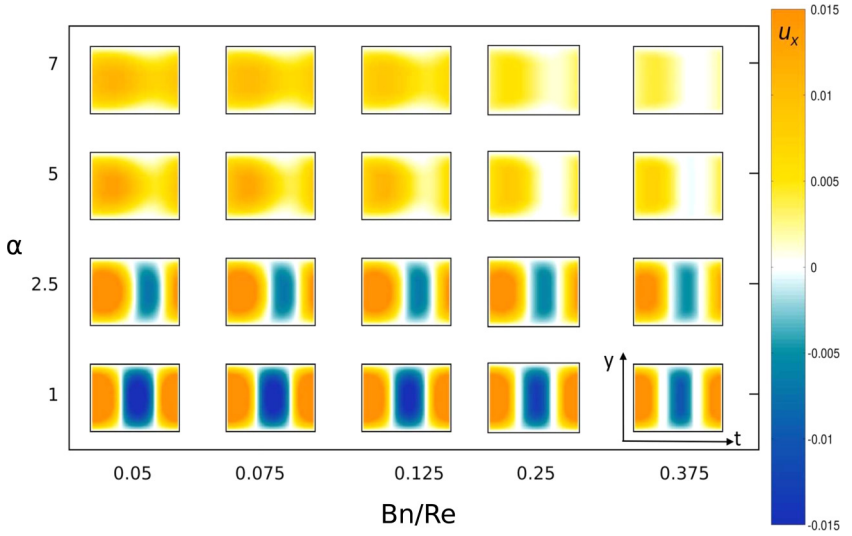

FIG. 15. Space-time diagram of the velocity during one period of oscillation for each pair of α, Bn/Re and $n = 1.3$ (high-amplitude, low mean flow). For each subplot, the x axis corresponds to the temporal evolution, and the y axis is the position inside the channel.

time, and it periodically extends over the whole channel. For large values of α, small values of Bn/Re result in a nearly steady dynamics similar to that observed in the weakly oscillating case, and large values of Bn/Re lead to a strongly nonlinear dynamics with important phase shifts across the channel.

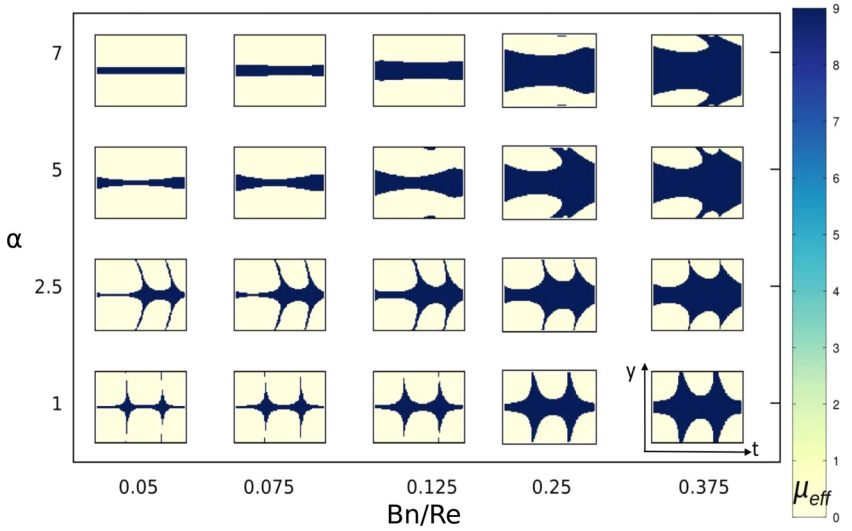

FIG. 16. Space-time diagram of the dynamic viscosity during one period of oscillation for each pair of α, Bn/Re and $n = 1.3$ (high-amplitude, low mean flow). For each subplot, the x axis corresponds to the temporal evolution, and the y axis is the position inside the channel. The blue part represents the "solid" behavior of the fluid, while the white part represents the liquid part.

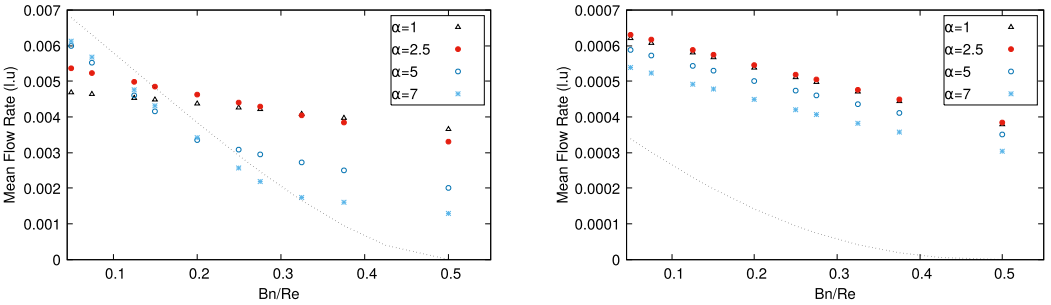

FIG. 17. (a) Mean flow rate for each pair of (α, Bn/Re) and $n = 1.3$. (b) Mean flow rate for each pair of (α, Bn/Re) and $n = 0.7$. Dotted line: flow rate for Poiseuille flow.

The nonlinear flow properties have a major effect on the time-averaged flow rate. This is examined in Figs. 17(a) and 17(b), where it is noted that the flow rate can substantially depart from the linear flow rate, i.e., the flow rate resulting from the time-averaged driving force. The effect of the force fluctuations on the flow rate depends on the oscillation frequency and fluid properties. In the shear-thickening case ($n = 1.3$), force fluctuations tend do decrease the flow rate for small values of Bn/Re. The largest flow rate is thus obtained for large values of α, i.e., in the case where the fluctuating part of the flow is small. A regime transition occurs between Bn/Re $= 0.1$ and Bn/Re $= 0.2$; for large values of Bn/Re, force fluctuations result in a major increase of the flow rate. Largest flow rates are achieved when the pulsation rate is small, indicating that this amplification mechanism might be mostly related to a pseudostatic effect. In fact, the amplification mechanism can be understood by considering the case Bn/Re $= 0.5$ as an illustrative example. For this value of Bn/Re, the time-averaged body force is not strong enough to overcome the yield stress; therefore, the corresponding steady flow rate is equal to zero in Fig. 17(a). However, force fluctuations may be large enough to produce an instantaneous flow. In particular, positive force fluctuations, whose amplitude is added to the positive mean force, are likely to produce a positive flow. In contrast, negative force fluctuations that are opposed to the mean force must achieve higher amplitudes to overcome the yield stress, and they may even not be able to produce any negative flow, as seen in Fig. 15 for $\alpha = 7$ and Bn/Re $= 0.375$. This *ratchet* process resulting from the yield-stress property thus provides a simple mechanism that substantially increases the mean-flow rate through flow oscillations. A similar phenomenon is observed for the shear-thinning case shown in Fig. 17(b). However, no regime transition is observed in this case: the flow rate amplification mechanism is observed for all values of Bn/Re. Moreover, the maximal flow rate is achieved for $\alpha = 2.5$, suggesting the existence of an optimal pulsation rate maximizing the fluid transport.

The phase difference between the oscillatory force and the instantaneous flow rate is plotted in Fig. 18 for the shear-thickening case. The phase difference is mostly determined by the pulsation rate; similarly to the Newtonian case, the phase lag increases as a function of α. The phase difference also slightly decreases as a function of Bn/Re. This trend is similar to that observed in the purely oscillating flow (see Fig. 11), even though less pronounced in this case.

The nonlinear flow response to the harmonic body forcing is clearly nonsinusoidal, as one can note in Figs. 15 and 16. This is further illustrated in Fig. 19(a), which shows the time evolution of the flow rate during one oscillation period. The nonharmonic form of the flow-rate signal is especially characterized by the emergence of quiescent-flow periods resulting from the yield-stress property of the fluid. In the Fourier space, these nonlinear effects are associated with the growth of higher harmonics in the flow spectrum. Figure 19(b) presents the evolution of the total higher-harmonic energy in the flow-rate spectrum normalized by total flow rate energy. Higher harmonics are defined as the spectral contributions associated with frequencies larger than f_0, where f_0 is

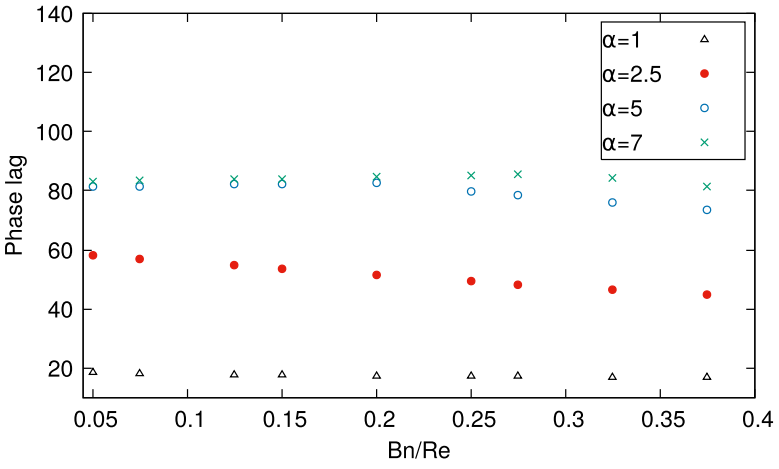

FIG. 18. Phase lag between force and flow rate response for each pair of (α, Bn/Re) and $n = 1.3$.

the fundamental frequency equal to the body force frequency. The energy growth is clearly noted as the flow nonlinearity increases. For low value of Bn/Re, the flow rate is close to the sinusoid, so the energy in the harmonics is low. When the value of Bn/Re increases, the energy contained in the harmonics increases. For the case of $\alpha = 1$, the value increases significantly because the instantaneous flow rate becomes zero [Fig. 19(a)].

The flow-response spectrum is further analyzed in Fig. 20 for different values of Bn/Re and α. In each case, the spatial distribution of the velocity spectrum is presented. At each position y/H, the spectral magnitude is normalized by the amplitude of the fundamental mode. As expected, the higher-harmonic frequency content tends to develop as Bn/Re increases; in particular, the frequency content becomes broader and the higher-harmonic amplitudes increase. In contrast, high-frequency contributions tend to decrease at large pulsation rates. As already discussed, the whole fluctuating part of the flow tends to vanish when the pulsation rate increases as an effect of fluid inertia. Here one can see that this inertial damping behaves as a low-pass filtering process, where higher harmonics are damped faster than the fundamental component. The same mechanism may explain the space-dependent frequency content observed in Fig. 20. The largest high-frequency modes tend to appear close to the channel walls, where the flow is dominated by viscous stresses. In contrast, the central region of the channel, which is dominated by inertia, exhibits smaller harmonics. These features might be important in systems where complex interactions can occur between the flow and the

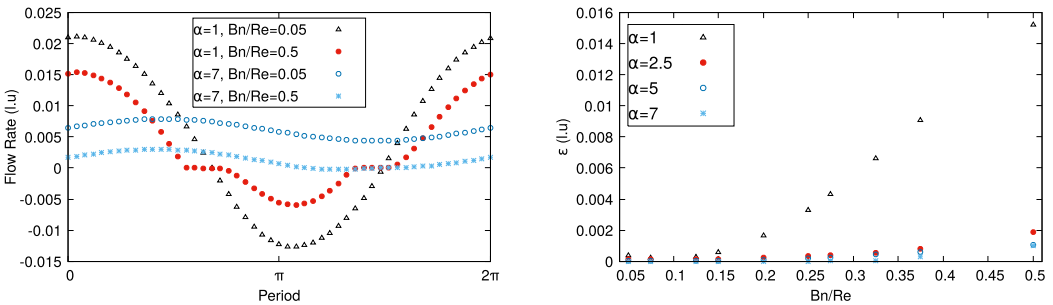

FIG. 19. (a) Flow rate over one period for $n = 1.3$. (b) Energy of harmonic frequency modes for various pairs (α, Bn/Re) and $n = 1.3$.

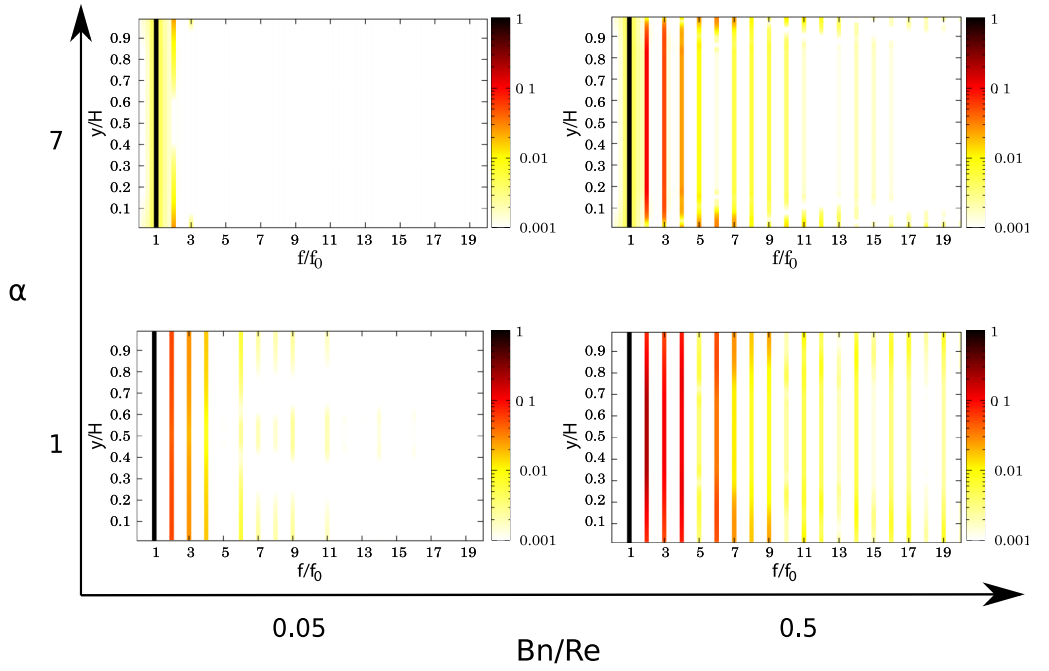

FIG. 20. Space-frequency diagrams of the spectral energy on the velocity for each pair of α, Bn/Re for $n = 1.3$. The x axis corresponds to the dimensionless frequency, and the y axis is the position inside the channel.

no-slip walls, e.g., in the presence of elastic boundaries. Moreover, the harmonic analysis may allow us to develop a tool to modify the sinusoidal forcing to a more complex signal that will optimize the mucociliary clearance, for example, by minimizing the period when the mucus is in its solid state.

VI. CONCLUSIONS

A parametric study of a pulsated Herschel-Bulkley fluid flow in a two-dimensional channel has been carried out using a lattice-Boltzmann method, addressing three configurations: purely oscillating flow, weakly oscillating flow, and strongly oscillating flow. The effects of the yield stress, through Bn/Re, and of the forcing signal frequency, through the Womersley number α, are characterized thoroughly.

The purely oscillating case illustrates the typical effects of force fluctuations on the non-Newtonian flow dynamics: a time-dependent solid plug which may extend across the whole channel and stop the flow, and strong phase differences in velocity and viscosity signals across the channel and inertial damping of high-frequency oscillations. The yield stress can strongly alter these effects, especially by controlling the typical size of the solid plug in the channel. When a time-averaged contribution is added to the body force, different dynamics can be observed depending on the relative magnitude of the fluctuating force. In the weakly oscillating case, the force fluctuations result in variations of the flow structure (e.g., a time-dependent plug at the center of the channel), but the global time-averaged flow dynamics remains mostly unaltered; in particular, the time-averaged flow rate is determined by the mean force component. In contrast, nonlinear effects are considerable in the strongly oscillating case. At large Bingham numbers, a simple *ratchet* mechanism resulting from the yield-stress property drives a major amplification of the mean flow. The nonlinear flow dynamics is also associated with the emergence of high-amplitude nonharmonic contributions in the flow-response spectrum, especially in the vicinity of the channel walls.

In the context of mouth pressure generator devices to assist patients in evacuating the mucus contained in their airways, this first parametric study allows one to identify some important aspects of the expected flow when the dynamics is governed by the yield stress and shear-thinning/thickening properties of the fluid. In particular, future developments will be oriented towards the control of the *ratchet* mechanism discussed above. The frequency content of the flow response might also be important in more complex systems involving time-dependent fluid properties and/or elastic walls. These systems will be addressed in future works.

ACKNOWLEDGMENTS

The authors acknowledge the Physio-Assist Company and the "Association Nationale de la Recherche et de la Technologie" for the CIFRE Grant No. 2018-0982 (A.G). The Centre de Calcul Intensif d'Aix-Marseille University is acknowledged for granting access to its high-performance computing resources.

APPENDIX: CASE OF THE SHEAR THINNING FLOW $n = 0.7$

1. Purely oscillating flow

Figures 21 and 22 represent the evolution of the velocity and the viscosity for $n = 0.7$. The increase in yield stress has the same impact on viscosity and velocity in the case of shear-thinning flows ($n = 0.7$) as in the case of shear-thickening flows ($n = 1.3$). Indeed, when Bn/Re increases, the duration when the channel is totally obstructed increases and the viscosity is equal to that of the "solid."

The evolution of the phase lag, shown in Fig. 23, is the same as in the case of a shear-thickening flow. Indeed, when the yield stress increases, the value of the phase lag decreases [for example, for $\alpha = 2.5$, the value goes from 7 (Bn/Re $= 0.05$) to 0 (Bn/Re $= 0.375$)]. However, the value is always lower for the same parameters in the shear-thinning case than in the shear-thickening case (see Fig. 11).

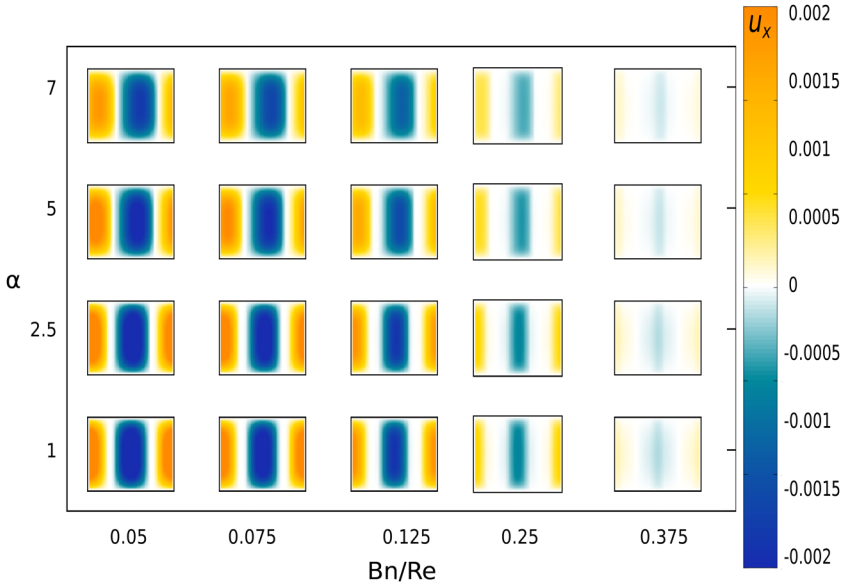

FIG. 21. Space-time diagram of the velocity field during one period for each pair of dimensionless numbers α, Bn/Re and $n = 0.7$. The velocity magnitude is indicated by the color bar. For each subplot, the x axis corresponds to the temporal evolution, and the y axis gives the position inside the channel.

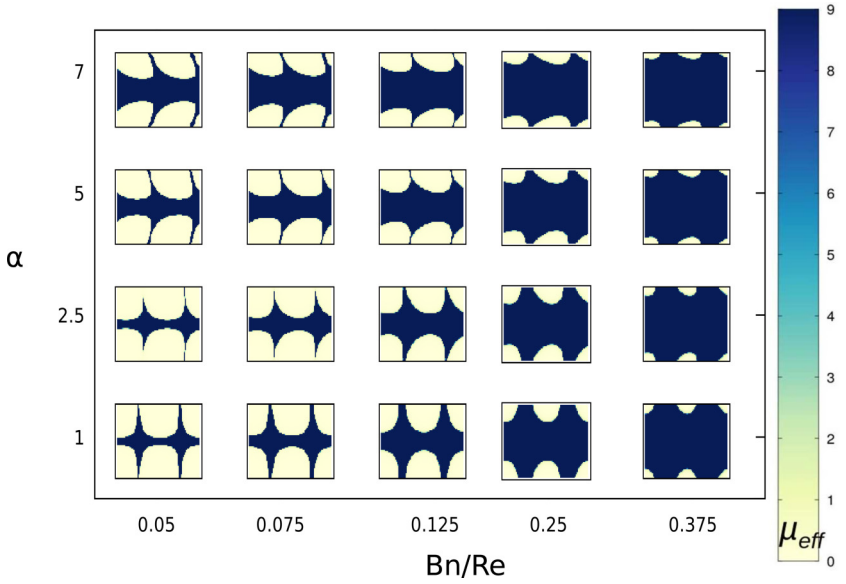

FIG. 22. Space-time diagrams of dynamic viscosity during one period for each pair of dimensionless numbers α, Bn/Re and $n = 0.7$. For each subplot, the x axis corresponds to the temporal evolution, and the y axis gives the position inside the channel. The blue part represents the "solid" behavior of the fluid, while the white part represents the liquid part.

2. Weakly oscillating flow

The time evolutions of the flow velocity and viscosity are shown in Figs. 24 and 25 respectively. The flow remains always positive for all configurations. The effect of α and Bn/Re on the velocity and the viscosity is identical to the shear-thickening case (see Figs. 12 and 13).

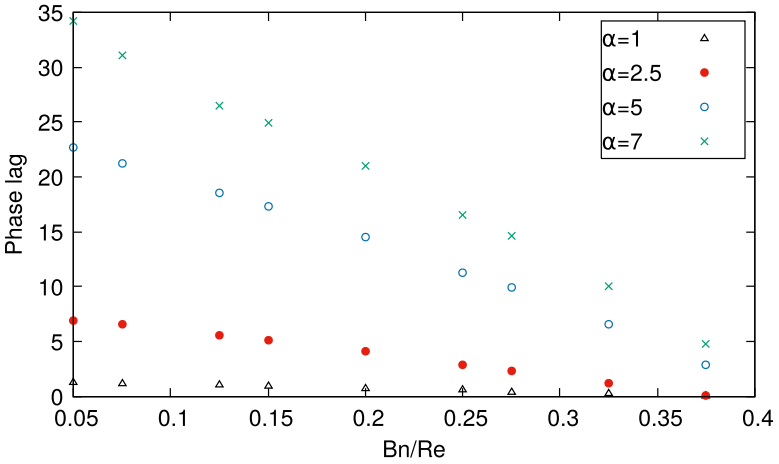

FIG. 23. Phase lag (in degrees) between the driving force and the flow rate for each pair of (α, Bn/Re) and $n = 0.7$.

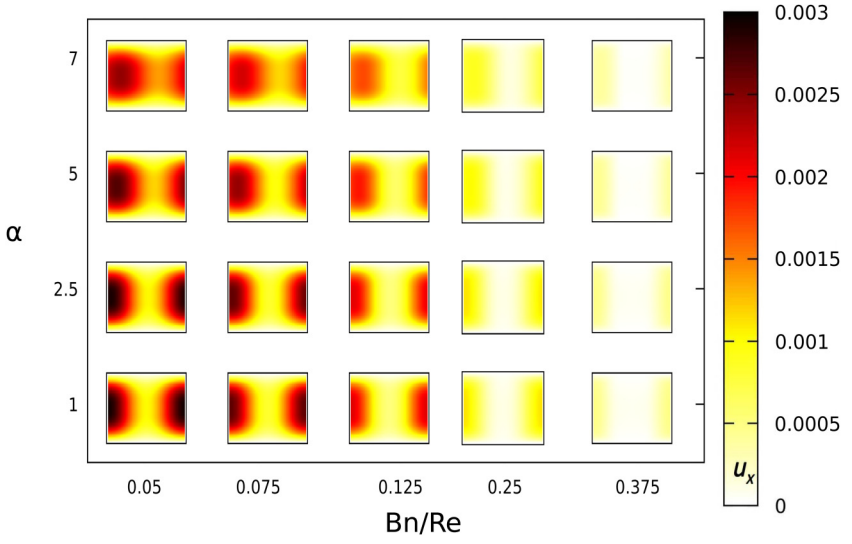

FIG. 24. Space-time diagram of the velocity field during one period for each pair of dimensionless numbers α, Bn/Re, and $n = 0.7$. The velocity magnitude is indicated by the color bar. For each subplot, the x axis corresponds to the temporal evolution, and the y axis gives the position inside the channel.

3. Strongly oscillating flow

Figures 26 and 27 represent the evolution of the velocity and the viscosity for $n = 0.7$. In the case of a shear-thinning flow, it is impossible to make the flow unidirectional when the value of $\mathrm{Re} = 0.1$. The impact of the increase in the value of α is weaker than in the case of a shear-thickening flow.

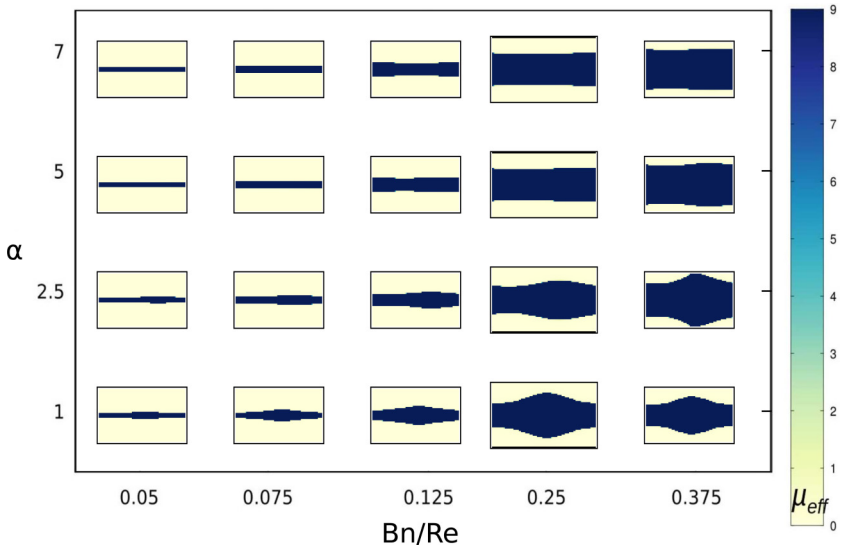

FIG. 25. Space-time diagrams of dynamic viscosity during one period for each pair of dimensionless numbers α, Bn/Re, and $n = 0.7$. For each subplot, the x axis corresponds to the temporal evolution, and the y axis gives the position inside the channel. The blue part represents the "solid" behavior of the fluid, while the white part represents the liquid part.

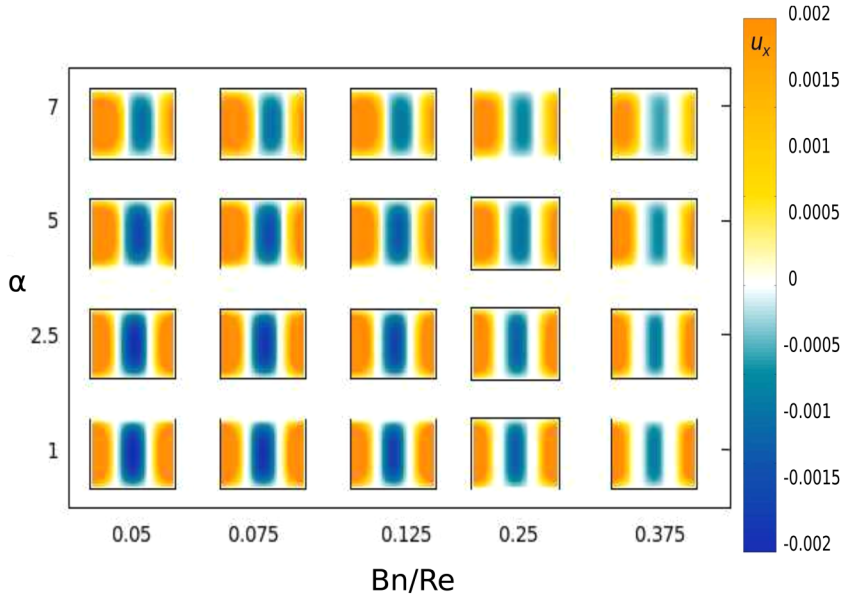

FIG. 26. Space-time diagram of the velocity field during one period for each pair of dimensionless numbers α, Bn/Re and $n = 0.7$. The velocity magnitude is indicated by the color bar. For each subplot, the x axis corresponds to the temporal evolution, and the y axis gives the position inside the channel.

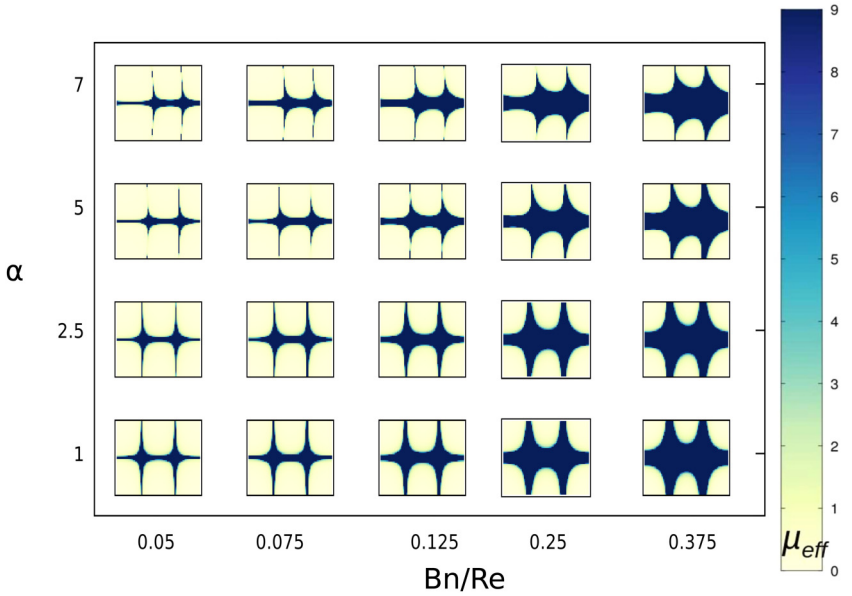

FIG. 27. Space-time diagrams of dynamic viscosity during one period for each pair of dimensionless numbers α, Bn/Re and $n = 0.7$. For each subplot, the x axis corresponds to the temporal evolution, and the y axis gives the position inside the channel. The blue part represents the "solid" behavior of the fluid, while the white part represents the liquid part.

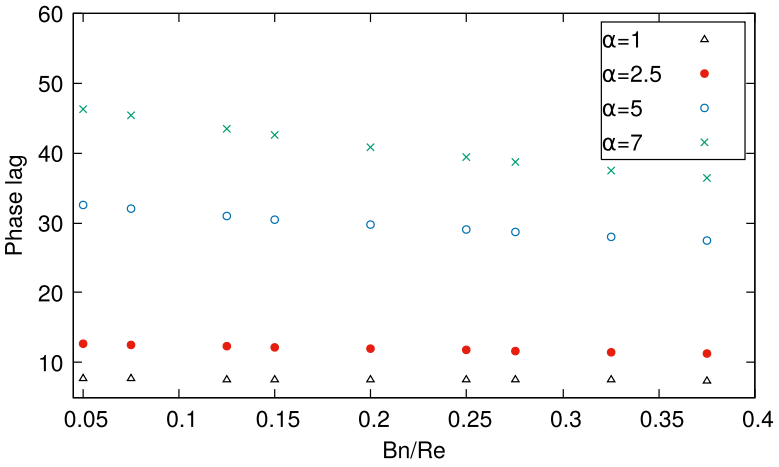

FIG. 28. Phase lag between force and flow rate response for each pair of (α, Bn/Re) and $n = 0.7$.

Indeed, the channel is blocked in all configurations whereas in the shear-thickening case a plug flow develops for $\alpha > 5$ and Bn/Re > 0.25.

Figure 28 shows that the phase lag decreases with Bn/Re for all the values of α whereas in the shear-thickening case, the phase lag increases slightly for the $\alpha = 5$ and $\alpha = 7$ cases. Moreover, the value of the phase lag is always lower in the shear-thinning case than in the shear-thickening case.

Figure 29(a) shows the flow rate vs time over an oscillation. As Bn/Re increases, the evolution of the flow rate for $\alpha = 1$ is comparable to that of a shear-thickening flow. The increase of the pulsation frequency does not allow to have a flow signal close to a sinusoidal signal. We can therefore see in Fig. 29(b) that the energy contained in the harmonics is greater than in the shear-thickening case.

Figure 30 corresponds to the same plot as Fig. 20 but in the case $n = 0.7$. Unlike the latter, Fig. 30 does not allow us to say that the energy contained in the high harmonics increases with the increase in the value of Bn/Re. In the case $\alpha = 1$, the energy contained in the high harmonics ($f/f_0 > 6$) seems to decrease with the increase of Bn/Re. However, for the first harmonics ($f/f_0 < 6$) the energy increases with Bn/Re. Moreover, the inertia-dominated central region of the channel exhibits smaller harmonics as for $n = 1.3$. Then we notice that the energy decreases with the increase of α and is distributed in the first harmonics. However, when the value of Bn/Re increases, we notice an evolution of the frequency distribution identical to the case $n = 1.3$.

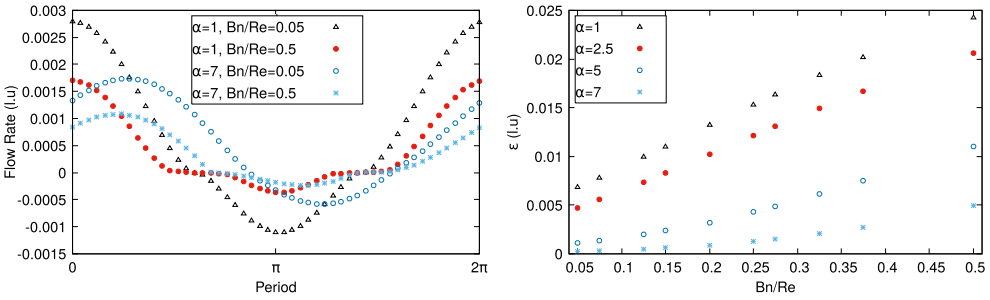

FIG. 29. (a) Flow rate over one period for $n = 0.7$. (b) Energy of harmonic frequency modes for various pairs (α, Bn/Re) and $n = 0.7$.

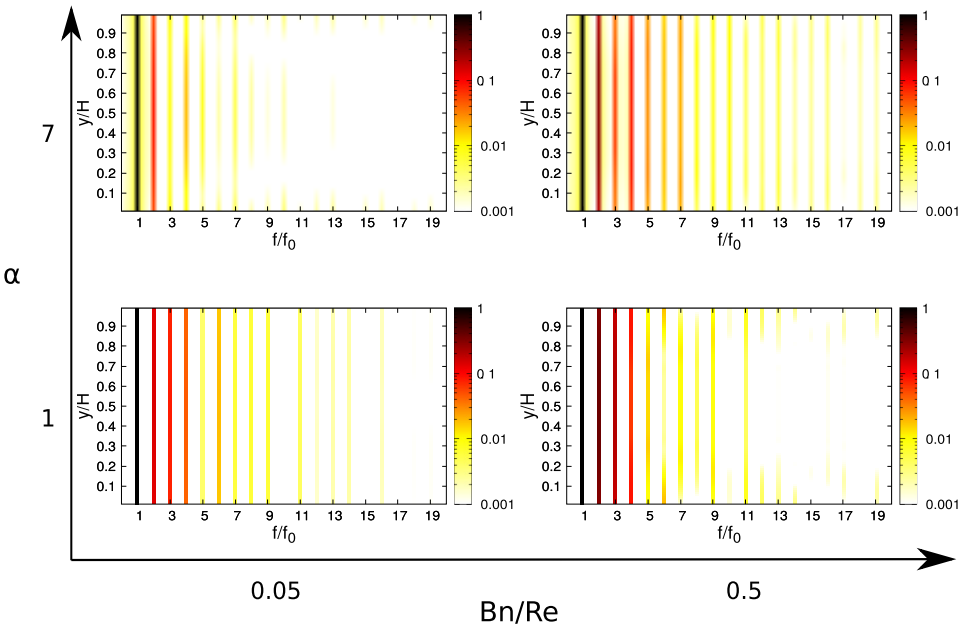

FIG. 30. Space-time diagrams of the spectral energy on the velocity for each pair of α, Bn/Re for $n = 0.7$. The x axis corresponds to the dimensionless frequency, and the y axis is the position inside the channel.

[1] M. Chilvers and C. O'Callaghan, Local mucociliary defence mechanisms, Paediatric Respir. Rev. **1**, 27 (2000).

[2] M. R. Knowles and R. C. Boucher, Mucus clearance as a primary innate defense mechanism for mammalian airways, J. Clin. Invest. **109**, 571 (2002).

[3] D. R. Strombeck and D. Harrold, Binding of cholera toxin to mucins and inhibition by gastric mucin, Infect. Immun. **10**, 1266 (1974).

[4] M. Bottier, M. Peña Fernández, G. Pelle, D. Isabey, B. Louis, J. B. Grotberg, and M. Filoche, A new index for characterizing micro-bead motion in a flow induced by ciliary beating: Part II, Modeling, PLoS Comput. Biol. **13**, e1005552 (2017).

[5] S. Chateau, J. Favier, U. D'Ortona, and S. Poncet, Transport efficiency of metachronal waves in 3D cilium arrays immersed in a two-phase flow, J. Fluid Mech. **824**, 931 (2017).

[6] R. C. Boucher, Airway surface dehydration in cystic fibrosis: Pathogenesis and therapy, Annu. Rev. Med. **58**, 157 (2007).

[7] M. Robinson and P. T. Bye, Mucociliary clearance in cystic fibrosis, Pediatr. Pulmonol. **33**, 293 (2002).

[8] D. Rogers and I. Doull, Physiological principles of airway clearance techniques used in the physiotherapy management of cystic fibrosis, Curr. Paediatrics **15**, 233 (2005).

[9] D. White, K. Stiller, and K. Willson, The role of thoracic expansion exercises during the active cycle of breathing techniques, Physiotherapy Theory Practice **13**, 155 (1997).

[10] C. M. Oermann, M. M. Sockrider, D. Giles, M. K. Sontag, F. J. Accurso, and R. G. Castile, Comparison of high-frequency chest wall oscillation and oscillating positive expiratory pressure in the home management of cystic fibrosis: A pilot study, Pediatr. Pulmonol. **32**, 372 (2001).

[11] Physio-Assist, https://www.physioassist.com/.

[12] J. Pryor, E. Tannenbaum, S. Scott, J. Burgess, D. Cramer, K. Gyi, and M. Hodson, Beyond postural drainage and percussion: Airway clearance in people with cystic fibrosis, J. Cystic Fibrosis **9**, 187 (2010).

[13] O. Lafforgue, N. Bouguerra, S. Poncet, I. Seyssiecq, J. Favier, and S. Elkoun, Thermo-physical properties of synthetic mucus for the study of airway clearance, J. Biomed. Mater. Res. A **105**, 3025 (2017).
[14] O. Lafforgue, I. Seyssiecq, S. Poncet, and J. Favier, Rheological properties of synthetic mucus for airway clearance, J. Biomed. Mater. Res. A **106**, 386 (2018).
[15] V. Di Federico, S. Longo, S. King, L. Chiapponi, D. Petrolo, and V. Ciriello, Gravity-driven flow of Herschel–Bulkley fluid in a fracture and in a 2D porous medium, J. Fluid Mech. **821**, 59 (2017).
[16] R. Banerjee, J. R. Bellare, and R. Puniyani, Effect of phospholipid mixtures and surfactant formulations on rheology of polymeric gels, simulating mucus, at shear rates experienced in the tracheobronchial tree, Biochem. Eng. J. **7**, 195 (2001).
[17] C. T. Nordgård and K. I. Draget, Oligosaccharides as modulators of rheology in complex mucous systems, Biomacromolecules **12**, 3084 (2011).
[18] G. Tomaiuolo, G. Rusciano, S. Caserta, A. Carciati, V. Carnovale, P. Abete, A. Sasso, and S. Guido, A new method to improve the clinical evaluation of cystic fibrosis patients by mucus viscoelastic properties, PLoS ONE **9**, e82297 (2014).
[19] M. Dawson, D. Wirtz, and J. Hanes, Enhanced viscoelasticity of human cystic fibrotic sputum correlates with increasing microheterogeneity in particle transport, J. Biol. Chem. **278**, 50393 (2003).
[20] S. K. Lai, Y.-Y. Wang, D. Wirtz, and J. Hanes, Micro-and macrorheology of mucus, Adv. Drug Delivery Rev. **61**, 86 (2009).
[21] Y. S. Park and P. L.-F. Liu, Oscillatory pipe flows of a yield-stress fluid, J. Fluid Mech. **658**, 211 (2010).
[22] D. Sankar and K. Hemalatha, Pulsatile flow of Herschel–Bulkley fluid through catheterized arteries—A mathematical model, Appl. Math. Model. **31**, 1497 (2007).
[23] D. Sankar and U. Lee, Mathematical modeling of pulsatile flow of non-Newtonian fluid in stenosed arteries, Comm. Nonlinear Sci. Numer. Sim. **14**, 2971 (2009).
[24] T. C. Papanastasiou, Flows of materials with yield, J. Rheol. **31**, 385 (1987).
[25] R. B. Bird, G. C. Dai, and J. B. Yarusso, The rheology and flow of viscoplastic materials, Rev. Chem. Eng. **1**, 1 (1983).
[26] J. R. Womersley, Method for the calculation of velocity, rate of flow and viscous drag in arteries when the pressure gradient is known, J. Physiol. **127**, 553 (1955).
[27] Z. Guo, C. Zheng, and B. Shi, Discrete lattice effects on the forcing term in the lattice Boltzmann method, Phys. Rev. E **65**, 046308 (2002).
[28] S. Gsell, U. D'Ortona, and J. Favier, Lattice-Boltzmann simulation of creeping generalized Newtonian flows: Theory and guidelines, J. Comput. Phys. **429**, 109943 (2021).
[29] D. d'Humières and I. Ginzburg, Viscosity independent numerical errors for lattice Boltzmann models: From recurrence equations to "magic" collision numbers, Comput. Math. Appl. **58**, 823 (2009).
[30] I. Ginzburg, D. d'Humières, and A. Kuzmin, Optimal stability of advection-diffusion lattice Boltzmann models with two relaxation times for positive/negative equilibrium, J. Stat. Phys. **139**, 1090 (2010).
[31] T. Krüger, H. Kusumaatmaja, A. Kuzmin, O. Shardt, G. Silva, and E. M. Viggen, *The Lattice Boltzmann Method - Principles and Practice* (Springer International Publishing, 2017).
[32] Q. Zou and X. He, On pressure and velocity boundary conditions for the lattice Boltzmann BGK model, Phys. Fluids **9**, 1591 (1997).